Reaction front development from ignition spots in *n*-heptane/air mixtures: Low-temperature chemistry effects induced by ultrafine water droplet evaporation

Zhou Yu (于洲), and Huangwei Zhang (张黄伟)[a] [ID]

AFFILIATIONS

Department of Mechanical Engineering, National University of Singapore, 9 Engineering Drive 1, Singapore 117576

[a]Author to whom correspondence should be addressed: huangwei.zhang@nus.edu.sg

ABSTRACT

Effects of low-temperature chemistry induced by ultrafine water droplet evaporation on reaction front development from an ignition spot with temperature gradient are studied in this work. The Eulerian–Eulerian method is used to simulate the gas–liquid two-phase reactive flows, and the physical model is one-dimensional spherical reactor with stoichiometric gaseous *n*-heptane/air mixture and ultrafine monodisperse water droplets (initial diameter 5 μm). Homogeneous ignitions of two-phase mixtures are first simulated. The water droplets can completely evaporate in the reactor prior to ignition, and hence pronouncedly reduce gas temperature, which may induce the low-chemistry reactions. It is found that the turnover temperature for negative temperature coefficient range increases with droplet volume fraction. Three-stage ignitions are present when the volume fraction is beyond a critical value, that is, low-temperature, intermediate-temperature, and high-temperature ignitions. The chemical explosive mode analysis also confirms the low-chemistry reactions induced by the evaporation of ultrafine water droplets. Then, reaction front development from an ignition spot with temperature gradient in two-phase mixtures is analyzed based on one-dimensional simulations. Different modes for reaction front origin in the spot are identified, based on the initial gas temperature and lower turnover temperature. Specifically, the reaction front can be initiated at the left and right ends of the ignition spot, and inside it. Detailed reaction front developments corresponding to the above three modes are discussed. In addition, the pressure wave from high-temperature ignition is important, compared to those from low and intermediate chemistries. The reaction front propagation speed and thermal states of fluid particles corresponding to different reaction front initiation modes are analyzed. Moreover, autoignition modes are summarized in the diagrams of normalized temperature gradient vs normal acoustic time and droplet volume fraction. The detonation limits of two-phase mixtures highly depend on the droplet volume fraction and are not regularly peninsular-shaped, like those for purely gaseous mixtures.

Published under an exclusive license by AIP Publishing. https://doi.org/10.1063/5.0061486

I. INTRODUCTION

Downsizing of spark-ignition (SI) engines with turbocharging technology is promising, since it is deemed a novel solution for pollutant reduction and fuel economy.[1] However, knocking combustion is likely to happen,[2–5] caused by the interactions between acoustic wave and chemical reaction when end gas autoignites.[1,6] In particular, detonation development (i.e., the interaction between supersonic shock wave and exothermic chemical reaction in a detonable medium[7–9]) in superknock subject to localized reactivity non-uniformity (e.g., temperature gradient) in the chamber plays a dominant role in inducing this hazardous phenomenon.[10,11]

Zeldovich[12] identified different autoignition modes caused by a hot spot with thermal inhomogeneity, that is, subsonic reaction wave, detonation development, and supersonic reaction wave. Bradley and his co-workers[13–16] further introduced a detonation peninsula (termed as *Bradley's diagram* hereafter), parameterized by normalized temperature gradient ξ and normalized acoustic time ε. After that, numerous simulations have been performed to uncover the underpinning mechanism of autoignition and detonation development from a localized ignition spot.[17–31] For instance, Dai *et al.*[24–28] investigated the various effects on autoignition and detonation development in dimethyl ether (DME)/air and *n*-C$_7$H$_{16}$/air mixtures under engine-relevant

conditions. It is noted that multi-stage ignition occurs at low initial temperature for large hydrocarbon fuels. In Ref. 25, Dai and Chen found that the temperature gradient of the hot spot is able to affect the interactions between multi-stage ignition and pressure waves. Pan et al.[19] studied the role of low temperature chemistry in combustion mode development and autoignition position. Moreover, Terashima et al.[21–23] unveiled the mechanisms of pressure wave development in end-gas autoignition during knocking combustion. They also found that both the amplitude of pressure oscillations and timing of knocking occurrence are affected by low-temperature chemistry and strong pressure wave is induced by a hot spot with high reactivity. In addition to the above one-dimensional simulations, the effects of inhomogeneities of thermochemical conditions (e.g., temperature or composition) on autoignition and knock formation were also investigated by Luong et al.[32,33] with multi-dimensional simulations. It is shown that reduction of energetic length scale would be helpful for mitigating knocking propensity. They introduced two parameters to predict the knocking intensity, that is, detonation propensity and heat release rate fraction, which show good correlations with the knock intensity when they are plotted against the normalized acoustic time ε.

It is well known that water injection technology is an effective approach to mitigate or alleviate knock in internal combustion (IC) engines.[34–37] This is because evaporation of liquid water can reduce the in-cylinder temperature, because of high latent heat of vaporization and specific heat capacity of water vapor.[34,38] This technology has been vigorously studied in recent years. For instance, Wang et al.[37] investigated the possibility of injected water to extend the knock limits of a spark-ignition engine fueled with kerosene. They found that the knock limit of their engine is significantly extended via water injection. In addition, Miganakallu et al.[39] studied the effects of liquid water/methanol injection on engine borderline knock conditions. They observed that the addition of water in the fuel blends promotes combustion stability and considerably reduces the gas temperature. Zhuang et al.[40] also investigated the benefits of water injection on downsized boosted SI engine and pointed out that the water injection can effectively reduce the NO and CO emissions with increased injected water percentage.

Numerical simulations on the effects of droplets including water and fuel sprays on shock wave propagation and detonation development are also available.[41–43] Zhuang et al.[43] studied autoignition and detonation development due to a hot spot in n-C_7H_{16}/air mixtures with liquid water droplets. The influences of droplet diameter and number density on reactive front development were discussed. However, detonation development regime associated with thermochemical properties of the hot spot (e.g., excitation time and acoustic time) in water-containing mixtures was not studied therein. More recently, the effects of water steam dilution on autoignition and detonation development induced by ignition spot with thermal inhomogeneity in n-C_7H_{16}/air mixture was numerically investigated in our previous work.[44] However, in situ water droplet evaporation during reaction front development is not considered, and therefore, how it affects initiation of the chemical reactions (such as low-temperature chemistry) of complex hydrocarbon fuels (e.g., n-heptane) from the ignition spot is not clear.

In this study, detailed numerical simulations of reaction front development from an ignition spot with temperature gradient in two-phase medium will be conducted. The physical model is one-

dimensional spherical reactor filled with stoichiometric n-C_7H_{16}/air gas and ultrafine water droplets. The research objectives are as follows: (i) to study the low-temperature chemistry effects (caused by the ultrafine water droplet evaporative cooling) on reaction front development, (ii) to identify the reaction front initiation mode subject to different droplet and gas properties, and (iii) to discuss the applicability of Bradley's diagram for the studied two-phase mixtures. The rest of the paper is structured as below. Sections II and III introduce the mathematical and physical models and data analysis method. Homogeneous ignition in two-phase mixtures is analyzed in Sec. IV. One-dimensional simulations of autoignition and detonation development due to ignition spot are studied in Sec. V. Finally, Sec. VI summarizes the main conclusions.

II. MATHEMATICAL AND PHYSICAL MODELS
A. Gas phase equation

The governing equations of momentum, energy, and species mass fraction are solved for one-dimensional unsteady, multi-component, reacting flows. They can be written in a spherical coordinate as

$$\frac{\partial U}{\partial t} + \frac{\partial F(U)}{\partial r} + 2\frac{G(U)}{r} = F_v(U) + S_R + S_L, \tag{1}$$

where t and r are time and radial coordinate, respectively. The vectors U, $F(U)$, $F_v(U)$, $G(U)$, S_R and S_L, respectively, have the following expressions:

$$U = \begin{bmatrix} \rho Y_1 \\ \rho Y_2 \\ \vdots \\ \rho Y_n \\ \rho u \\ E \end{bmatrix}, \quad F(U) = \begin{bmatrix} \rho u Y_1 \\ \rho u Y_2 \\ \vdots \\ \rho u Y_n \\ \rho u^2 + P \\ (E+P)u \end{bmatrix}, \quad G(U) = \begin{bmatrix} \rho u Y_1 \\ \rho u Y_2 \\ \vdots \\ \rho u Y_n \\ \rho u^2 \\ (E+P)u \end{bmatrix},$$

$$F_v(U) = \begin{bmatrix} -r^{-2}(r^2 \rho Y_1 V_1')_r \\ -r^{-2}(r^2 \rho Y_2 V_2')_r \\ \vdots \\ -r^{-2}(r^2 \rho Y_n V_n')_r \\ r^{-2}(r^2 \tau_1)_r - 2\tau_2/r \\ r^{-2}q_r + \Phi \end{bmatrix}, \quad S_R = \begin{bmatrix} \omega_1 \\ \omega_2 \\ \vdots \\ \omega_n \\ 0 \\ 0 \end{bmatrix}, \quad S_L = \begin{bmatrix} S_{m,1} \\ S_{m,2} \\ \vdots \\ S_{m,n} \\ S_v \\ S_e \end{bmatrix}. \tag{2}$$

ρ is the density and u is the radial velocity. $E \equiv -P + \rho u^2/2 + \rho h$ is the total energy, with h being the total enthalpy. P is the pressure, obtained from the ideal gas equation of state $P = \rho R T/\overline{M}$. R is the universal gas constant, and T and $\overline{M}$ are the temperature and mean molecular weight of the gaseous mixture, respectively. Y_i and ω_i are the mass fraction and chemical reaction rate of ith species, respectively. n is the total number of species. The diffusion

velocity V_i' is determined using the mixture-averaged method. The chemical reaction rate ω_i, thermodynamic, and transport properties are calculated by CHEMKIN or TRANSPORT packages.[45,46] In Eq. (2), the subscript "r" in $F_v(U)$ stands for the partial derivative with respect to the spatial coordinate r. τ_1 and τ_2 are the viscous stresses, and q_r is the heat flux. In addition, Φ is the viscous dissipation rate. More details about the equations can be found in Refs. 28 and 47. The effects of water droplets on gaseous phase are taken into consideration through the source/sink terms S_L, and their expressions will be given in Eq. (19).

B. Liquid phase equation

The Eulerian approach is applied to describe the liquid droplet phase. Similar approach is also used by Sanjosé et al.,[48] Qiao et al.,[49] and Eidelman and Burcat[50,51] for gas–liquid and gas–solid two-phase flows. In this study, the water droplet is assumed to be spherical. The droplet temperature is uniform due to the approximation of droplet infinite thermal conductivity.[52,53] The droplet breakup and deformation are not considered due to the small droplet diameters. The evolution of droplet diameter is governed by

$$\frac{\partial d}{\partial t} + u_d \frac{\partial d}{\partial r} = -\frac{2\dot{m}}{\pi \rho_d d^2}, \tag{3}$$

where d, u_d, and ρ_d are the droplet diameter, velocity, and material density, respectively. The evaporation rate $\dot{m}$ is modeled as[54]

$$\dot{m} = \pi d \rho D_{water,m} Sh \ln(1 + B_M), \tag{4}$$

where $D_{water,m}$ is the binary diffusion coefficient of water vapor in the gaseous mixture and approximated following Ref. 55. The Sherwood number Sh is modeled as[54]

$$Sh = 2.0 + \frac{1}{F(B_M)}\left[(1 + Re_d Sc)^{1/3} \max(1, Re_d)^{0.077} - 1\right], \tag{5}$$

where $F(B) = \frac{\ln(1+B)}{B}(1+B)^{0.7}$ is used to model the change of film thickness due to Stefan flow effects.[54] The droplet Reynolds number Re_d is defined as

$$Re_d = \frac{\rho d |u - u_d|}{\mu}. \tag{6}$$

In Eq. (5), the Schmidt number Sc is estimated from

$$Sc = \frac{\mu}{\rho D_{water,m}}. \tag{7}$$

In Eqs. (4) and (5), B_M is the Spalding mass transfer number

$$B_M = \frac{Y_{ds} - Y_{d\infty}}{1 - Y_{ds}}, \tag{8}$$

where $Y_{d\infty}$ is the water vapor mass fraction in the bulk gas, and Y_{ds} is the water vapor mass fraction at the droplet surface

$$Y_{ds} = \frac{W_{H_2O} X_{ds}}{W_{H_2O} X_{ds} + (1 - X_{ds})\overline{W}}. \tag{9}$$

Here, W_{H_2O} is the water molecular weight and $\overline{W}$ is that of the gas-phase mixture (excluding H_2O vapor). X_{ds} is the water vapor mole fraction at the droplet surface

$$X_{ds} = \frac{P_{ref}}{P} \exp\left[\frac{L_v(T_{ref})}{R}\left(\frac{1}{T_{ref}} - \frac{1}{T_d}\right)\right]. \tag{10}$$

For water, the reference pressure is $P_{ref} = 1$ atm, the reference temperature is $T_{ref} = 370$ K, and the latent heat of vaporization is $L_v(T_{ref}) = 2260$ J/g. It is noted that T_{ref} is the corresponding boiling temperature under the reference pressure P_{ref}.

The equation of droplet velocity takes the following form:

$$\frac{\partial u_d}{\partial t} + u_d \frac{\partial u_d}{\partial r} = \frac{F_s}{m_d}. \tag{11}$$

Note that only drag force F_s is considered in our work and it is modeled using Schiller and Naumann's correlation,[56] that is, $F_s = \frac{m_d}{\tau_r} \cdot (u - u_d)$. $m_d = \rho_d \pi d^3 / 6$ is the mass of a single droplet. τ_r is the droplet momentum relaxation time and can be determined from[56]

$$\tau_r = \frac{\rho_d d^2}{18\mu}\frac{24}{C_d Re_d}, \tag{12}$$

where C_d is the drag coefficient[56]

$$C_d = \begin{cases} \dfrac{24}{Re_d}\left(1 + \dfrac{1}{6}Re_d^{2/3}\right) & \text{if } Re_d \le 1000, \\ 0.44 & \text{if } Re_d > 1000. \end{cases} \tag{13}$$

The studies by Cheatham and Kailasanath[57] confirm that Eq. (13) can accurately predict the gas velocity distributions in compressible two-phase flows.

The equation of droplet temperature reads

$$m_d C_{P,d}\left(\frac{\partial T_d}{\partial t} + u_d \frac{\partial T_d}{\partial r}\right) = h_c A_d (T - T_d) - \dot{m} L_v(T_d), \tag{14}$$

where $C_{P,d}$ is the constant pressure specific heat of the liquid phase and A_d is the surface aera of a single droplet. $L_v(T_d)$ is the latent heat of vaporization at the droplet temperature[58]

$$L_v(T_d) = d_1 \cdot (1 - T_r)^{[(d_2 \cdot T_r + d_3) \cdot T_r + d_4] \cdot T_r + d_5}, \tag{15}$$

where d_1, d_2, d_3, d_4, and d_5 are species-specific constants.[58] T_r is defined as $T_r = T_d / T_{cr}$, where T_{cr} is the critical temperature and is 647 K for water.

The convective heat transfer coefficient h_c is

$$h_c = \frac{Nu k_g}{d}, \tag{16}$$

where k_g is the thermal diffusivity of gas phase, and Nu is the Nusselt number and can be estimated with Ranz and Marshall model[59]

$$Nu = 2.0 + \frac{1}{F(B_T)}\left[(1 + Re_d Pr)^{1/3} \max(1, Re_d)^{0.077} - 1\right], \tag{17}$$

where $Pr = C_P \mu / k_g$ is the Prandtl number of the gas phase. $B_T = (1 + B_M)^{\varphi} - 1$ is the Spalding heat transfer number, in which $\varphi = (C_{p,v}/C_{P,d})/Le$. $Le \equiv \alpha/D$ (α is the thermal diffusivity, whilst D

is the mass diffusivity) is the Lewis number of the gaseous mixture and $C_{p,v}$ is the constant pressure specific heat of water vapor. The droplet heating and evaporation models are validated against with the single water droplet experiments (see the Appendix), and good accuracies are demonstrated about the evolutions of droplet diameter and temperature.

The equation of droplet number density N_d reads

$$\frac{\partial N_d}{\partial t} + \frac{\partial (N_d u_d)}{\partial r} + 2\frac{N_d u_d}{r} = 0. \tag{18}$$

In this study, two-way coupling between the gas and droplet phase is considered, characterized by the exchange of species, momentum, and energy. They correspond to the individual terms in S_L in Eq. (2)

$$\begin{cases} S_m = N_d \dot{m}, \\ S_v = -N_d m_d \dfrac{u - u_d}{\tau_r}, \\ S_e = -N_d h_c A_d (T - T_d) + N_d \dot{m}_d H_g(T_d). \end{cases} \tag{19}$$

S_m is non-zero only for the equation of H_2O mass fraction. $H_g(T_d)$ is the enthalpy of water vapor at droplet temperature.

We also would like to acknowledge the limitations of the Eulerian–Eulerian method include the following: (1) it is mainly suitable for dense droplet loading; (2) some critical droplet dynamics should be modeled if they are considered in the formulations, such as particle trajectory crossing; (3) solutions of Eulerian droplet equations for the dispersed phase normally are grid-dependent, which is particularly true for dilute spray regimes.

C. Physical model

The one-dimensional spherical reactor is shown in Fig. 1. The radius of the domain is $R = 4$ cm. For the gas phase, the initial distributions of pressure, velocity, and composition are uniform in the domain. Specifically, the initial pressure P_0 is 40 atm, and the initial temperature outside the ignition spot $T_{i,0}$ is 1000 K. They are chosen to mimic the high pressure and temperature in the end gas in internal combustion (IC) engine chambers.[1] The initial gas velocity is zero,
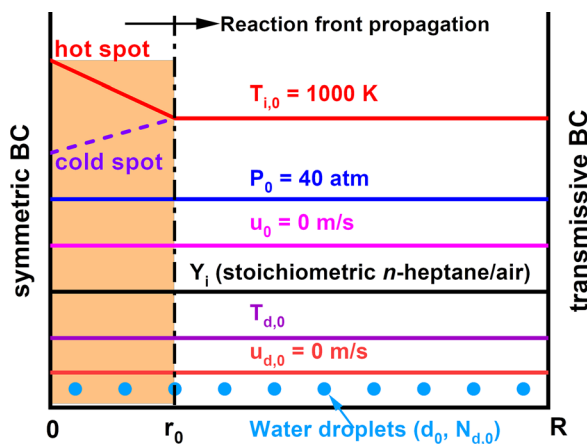
FIG. 1. Schematic of the one-dimensional spherical reactor.

that is, $u_0 = 0$ m/s. The reactor is filled with stoichiometric n-heptane/air mixture.

Dispersed ultrafine water droplets are considered to mimic the water mists injected into IC engine cylinder to mitigate the knock intensity and reduce pollutant emissions.[1,34–36] The water droplets are assumed to be mono-sized, and the initial droplet diameter is $d_0 = 5\,\mu$m. The initial droplet temperature and velocity are $T_{d,0} = 298$ K and $u_{d,0} = 0$ m/s, respectively. The density and constant pressure specific heat of water droplets are 1000 kg/m^3 and 4200 J/(kg K), respectively. Initially, they are uniformly distributed in the reactor and the number density $N_{d,0}$ is determined based on the initial droplet diameter d_0 and volume fraction $\alpha_{d,0}$, that is, $N_{d,0} = \alpha_{d,0}/\pi d_0{}^3/6$. Note that dilute droplet concentrations are studied here, and hence, the initial volume fraction $\alpha_{d,0}$ in our study is less than 1‰, following Crowe et al.[60]

The reactive front is initiated by an ignition spot with temperature gradient near the left boundary, and therefore, the initial temperature T_0 in the reactor is

$$T_0(r) = \begin{cases} T_{i,0} + (r - r_0)\dfrac{dT_0}{dr} & \text{for } 0 \leq r \leq r_0, \\ T_{i,0} & \text{for } r_0 < r \leq R, \end{cases} \tag{20}$$

where r_0 is the radius of the ignition spot, which is fixed to be 3.5 mm in this study. dT_0/dr is the initial temperature gradient inside the spot, which is constant and varied in our simulations. $T_{i,0}$ is the initial gas temperature beyond the spot, which is fixed to be 1000 K, close to the end gas temperature in IC engines.[20,29] Given that the negative temperature coefficient (NTC) phenomenon may occur due to droplet evaporation cooling, positive or negative initial temperature gradients dT_0/dr are used to initiate the autoigniting wave, which will be discussed in detail in Sec. IV.

The symmetric condition is enforced at $r = 0$, that is,

$$\begin{cases} u = 0, & \dfrac{\partial T}{\partial r} = \dfrac{\partial Y_i}{\partial r} = 0, \\ u_d = 0, & \dfrac{\partial d}{\partial r} = \dfrac{\partial T_d}{\partial r} = \dfrac{\partial N_d}{\partial r} = 0. \end{cases} \tag{21}$$

At $r = R$, the transmissive condition is used, that is,

$$\begin{cases} \dfrac{\partial u}{\partial r} = \dfrac{\partial T}{\partial r} = \dfrac{\partial Y_i}{\partial r} = 0, \\ \dfrac{\partial u_d}{\partial r} = \dfrac{\partial d}{\partial r} = \dfrac{\partial T_d}{\partial r} = \dfrac{\partial N_d}{\partial r} = 0. \end{cases} \tag{22}$$

D. Numerical implementation

The governing equations of gas and liquid phases are solved using a well-validated in-house code A-SURF (Adaptive Simulation of Unsteady Reactive Flow).[61] This has been proven to be an accurate tool for predicting shock and detonation waves.[18,24–28] The finite volume method is used to discretize the gas phase equations. The Strang splitting fractional-step procedure with second-order accuracy is adopted to separate the time evolution of reaction term S_R from that of the convection term $F(U)$, diffusion term $F_v(U)$, and source/sink term S_L to reduce the overall computational cost. For the liquid phase equations, the first-order accurate explicit Euler scheme is used for

temporal discretization. The second-order central differencing scheme is applied for convection terms. In addition, the source terms in Eqs. (3), (11), (14), and (18) are integrated explicitly.

Dynamically adaptive mesh refinement (AMR) algorithm[62] is used to capture the shock/reaction front, and the maximum level of refinement is assumed to 9. The minimum specific grid size is about $1.9\,\mu m$. It is found that further mesh refinement does not have influence of the reaction front evolutions (see Fig. S1 in the supplementary material). In addition, the time step is 5×10^{-11} s, which leads to Courant–Friedrichs–Lewy (CFL) number (based on gas properties) less than 0.4. Moreover, a skeletal n-C$_7$H$_{16}$ mechanism (44 species and 112 reactions)[63] with low-temperature chemistry is used and its capacity in predicting n-heptane detonation and low-temperature oxidation has been corroborated in previous studies.[24,25,28,43,44,64]

III. CHEMICAL EXPLOSIVE MODE ANALYSIS (CEMA)

The chemical explosive mode analysis (CEMA),[65–68] inspired by the computational singular perturbation method,[69,70] is used to extract the fundamental chemical state in reaction front development process. For a typical chemically reactive flow, the equations can be written as

$$\frac{D\boldsymbol{\varphi}}{Dt} = \boldsymbol{\omega}(\boldsymbol{\varphi}) + \boldsymbol{s}(\boldsymbol{\varphi}), \qquad (23)$$

where $D(\cdot)/Dt$ is the material derivative, $\boldsymbol{\varphi}$ is the vector of primary variables consisting of all species and temperature; that is, $\boldsymbol{\varphi} = [C_1, \ldots, C_n, T]$, C is the mass concentration. In the RHS of Eq. (23), $\boldsymbol{\omega}(\boldsymbol{\varphi})$ is the vector of the chemical source terms, whilst $\boldsymbol{s}(\boldsymbol{\varphi})$ is the vector of the non-chemical terms (e.g., diffusion). The CEMA is based on eigen analysis of the Jacobian matrix $\boldsymbol{J}_\omega$ of the chemical source term $\boldsymbol{\omega}(\boldsymbol{\varphi})$. A chemical mode is defined as an eigenmode of $\boldsymbol{J}_\omega$, which contains an eigenvalue and the corresponding eigenvectors. Furthermore, a CEM is the chemical mode whose real part of the eigenvalue λ_e is positive, that is, Re$(\lambda_e) > 0$. This indicates the propensity of chemical explosion when the mixture is isolated.

The contribution of a chemical species toward a CEM is quantified by the Explosion Index (EI)[67]

$$\mathbf{EI} = \frac{\text{diag}|\boldsymbol{a}_e \boldsymbol{b}_e|}{\text{sum}(\text{diag}|\boldsymbol{a}_e \boldsymbol{b}_e|)}, \qquad (24)$$

where $\boldsymbol{a}_e$ and $\boldsymbol{b}_e$ are, respectively, the right and left eigenvectors, and "diag$|\cdot|$" denotes the elementwise absolute values. The elements of $\mathbf{EI}$ range from 0 to 1. Similar EI can also be calculated for temperature. Higher $\mathbf{EI}$ value indicates higher contribution of the species or temperature in a CEM. In addition, the contribution of a reaction to a CEM is measured by the Participation Index (PI)[67]

$$\mathbf{PI} = \frac{|(\boldsymbol{b}_e \cdot \boldsymbol{S}) \otimes \boldsymbol{R}|}{\text{sum}(|(\boldsymbol{b}_e \cdot \boldsymbol{S}) \otimes \boldsymbol{R}|)}, \qquad (25)$$

where $\boldsymbol{S}$ is the stoichiometric coefficient matrix, $\boldsymbol{R}$ is the vector of net reaction rate, and "$\otimes$" represents the element-wise multiplication of two vectors. All the elements of $\mathbf{PI}$ lie within $[0, 1]$ and the reaction is dominant in the CEM if its PI is close to unity.

IV. HOMOGENEOUS IGNITIONS OF TWO-PHASE MIXTURES

To quantify the autoignition process in an ignition spot with temperature gradient, three parameters are used, that is, ignition delay time τ_{ig}, excitation time τ_e, and critical temperature gradient $(dT/dr)_c$.[14] Specifically, τ_{ig} is the duration when the heat release rate reaches its maximum from the initial instant, whilst τ_e denotes the time interval from 5% to maximum heat release.[14] Moreover, based on the theories by Zeldovich[12] and Gu $et\ al.$,[14] $(dT/dr)_c$ quantifies a critical temperature gradient within the ignition spot for chemical resonance and hence detonation development, that is,

$$\left(\frac{dT}{dr}\right)_c = \left[a\left(\frac{d\tau_{ig}}{dT_0}\right)\right]^{-1}, \qquad (26)$$

where $a = \sqrt{kR_g T}$ is the sound speed, k is the adiabatic index, and R_g is the gas constant. Under this temperature gradient, the reaction front from the ignition spot propagates at the speed of sound.

Homogeneous ignitions of stoichiometric n-C$_7$H$_{16}$/air mixtures with ultrafine water droplets in the 1D reactor in Fig. 1 will be discussed in Secs. IV A and IV B, to evaluate the effects of the droplet diameter and volume fraction on the above-mentioned parameters, that is, τ_{ig}, τ_e, and $(dT/dr)_c$. Here, all initial variables of gas and liquid phases are spatially uniform, thereby leading to zero-dimensional (0D) simulations in nature.

A. Homogeneous ignition process with droplets

Figure 2 shows the ignition delay time and critical temperature gradient of droplet-laden n-C$_7$H$_{16}$/air mixture vs gas temperature. The initial droplet volume fraction is $\alpha_{d,0} = 8.0 \times 10^{-4}$. The results from the droplet-free stoichiometric n-C$_7$H$_{16}$/air mixture are also included.
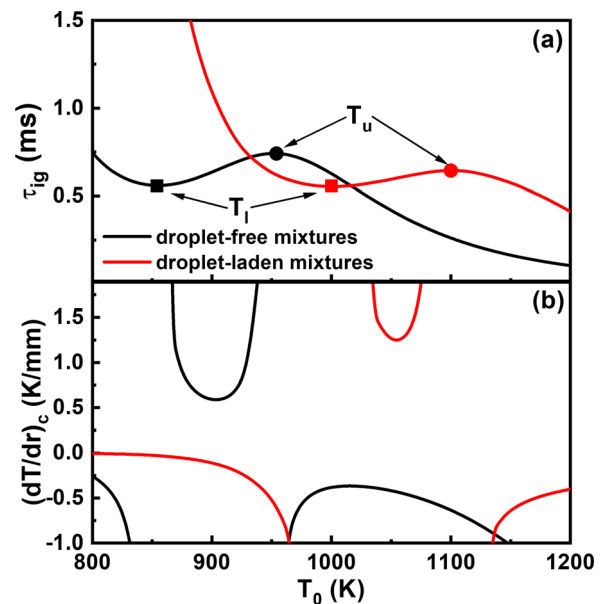
FIG. 2. (a) Ignition delay and (b) critical temperature gradient of stoichiometric n-C$_7$H$_{16}$/air mixtures with water droplets. $\alpha_{d,0} = 8.0 \times 10^{-4}$. T_u and T_l: upper and lower turnover temperature.

It is seen that the droplet addition considerably affects the dependence of τ_{ig} and $(dT/dr)_c$ on gas temperature. The turnover temperature [marked as symbols on Fig. 2(a)][71] is increased significantly in the two-phase mixtures compared to those of the droplet-free mixtures. Specifically, the lower turnover temperature is $T_l = 1000$ K, whereas the upper turnover temperature is $T_u = 1100$ K, larger than the counterparts (850 and 950 K) of droplet-free mixtures. Because of the NTC effects, the distributions of $(dT/dr)_c$ have three sections: middle positive branch and two lower negative ones, as shown in Fig. 2(b). A negative (positive) $(dT/dr)_c$ indicates that a hot (cold) spot is required for detonation development in 1D simulations.[27]

Figure 3 shows the time histories of temperature, pressure, heat release rate, and droplet diameter in homogeneous ignition of stoichiometric n-C_7H_{16}/air mixtures with water droplets. The initial volume fraction is 8.0×10^{-4}, and the initial temperature is 1000 K. One can see that, due to the heat absorption by water droplets, the gas temperature is reduced to a minimum value of 840.6 K at $t = 0.308$ ms, and the low-temperature chemistry is therefore initiated. Three ignition events are observed from the corresponding heat release peaks, respectively, at $t = 0.465$, 0.536, and 0.554 ms. They are, respectively, termed as low-, intermediate-, and high-temperature ignitions (abbreviated as LTI, ITI, and HTI).[25] It is noteworthy that the water droplets complete the evaporation at $t = 0.308$ ms, which is ahead of the onset of the LTI. Therefore, all the three ignition events occur in purely gaseous environment, although the initial mixture is laden with the ultrafine water droplets. It is noted that the heat release rate of each autoignition event is affected by both cooling (energy exchange) and dilution (mass exchange). The cooling is more important, since only dilution cannot lead to multi stage autoigntion.

In the above discussion, the droplet volume fraction is fixed to be 8.0×10^{-4} and its effects on n-C_7H_{16}/air autoignition will be further studied in Fig. 4, which shows the ignition delay time, droplet evaporation time, and turnover temperature with volume fractions of $0.005\%- 0.1\%$. For multi-stage autoignition, the ignition delay time of each stage is defined as the instant of maximum heat release with respect to the initial time, as shown in Fig. 3. $\tau_{ig,1}$, $\tau_{ig,2}$, and $\tau_{ig,3}$ (i.e., τ_{ig} in Fig. 2) are the corresponding ignition delay times for LTI, ITI, and HTI, respectively. The ignition delays of gaseous mixtures with
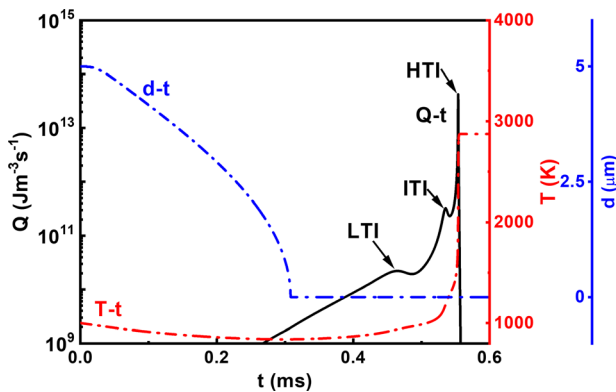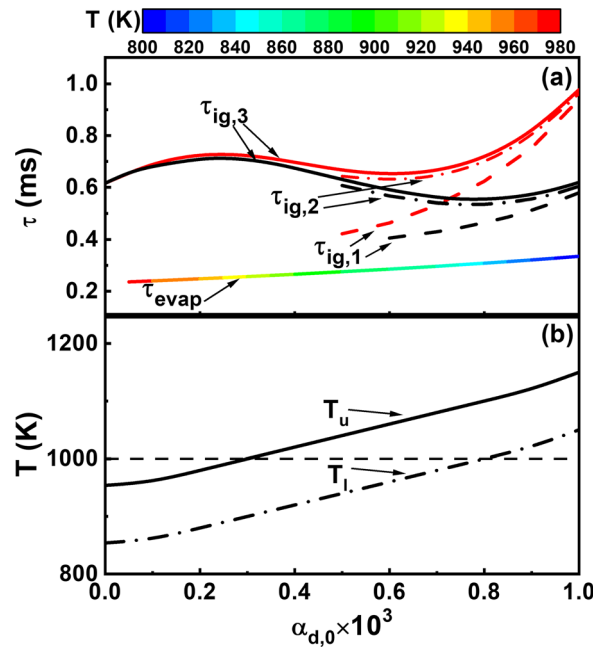
FIG. 4. (a) Ignition delay time and droplet evaporation time and (b) turnover temperature as functions of initial volume fraction. T_l is the lower turnover temperature, and T_u is the upper turnover temperature. $T_0 = 1000$ K. Black lines in (a) denote ignition delays of two-phase mixtures; red lines in (a) denote ignition delays of gaseous mixtures with the corresponding thermochemical states at the end of droplets evaporation.

the corresponding thermochemical states at the end of droplets evaporation (assumed infinite fast evaporation) are also shown. It is seen from Fig. 4(a) that the fine rate evaporation has a non-negligible on ignition delays, even if the droplets completely evaporate before LTI. This is because the moderate chemical reaction during the period of droplets evaporation. Further, only high-temperature ignition is observed when $\alpha_{d,0} < 5.0 \times 10^{-4}$. With $\alpha_{d,0} \geq 5.0 \times 10^{-4}$, multi-stage ignition appears. Increased $\alpha_{d,0}$ leads to monotonically increased $\tau_{ig,1}$. However, $\tau_{ig,2}$ and $\tau_{ig,3}$ show non-monotonic change with $\alpha_{d,0}$, indicating the NTC behaviors due to the water droplet evaporation. Moreover, the droplet evaporation time τ_{evap} is also shown, which corresponds to the instant when the droplet diameters in the reactor are reduced to $d \leq 10^{-12}$ μm (hence deemed complete evaporation). It is colored by the gas phase temperature. It is found that τ_{evap} is much smaller than the LTI delay for all the shown range of $\alpha_{d,0}$. This indicates that ignition proceeds in purely gaseous mixtures. The gas temperature when the droplets are fully vaporized in the reactor is also marked in the curve of τ_{evap}, and it ranges from 980 to 800 K when $\alpha_{d,0} < 1.0 \times 10^{-3}$. Moreover, it is seen from Fig. 4(b) that both lower and upper turnover temperatures increase with $\alpha_{d,0}$, implying that the NTC region moves toward higher temperature with increased $\alpha_{d,0}$. At about $\alpha_{d,0} = 8.0 \times 10^{-4}$, the value of T_l is close to the initial temperature of the gas mixture $T_0 = 1000$ K.

Figure 5 shows the excitation time τ_e and critical temperature gradient $(dT/dr)_c$ as functions of initial droplet volume fraction $\alpha_{d,0}$. To evaluate the water vapor dilution effects, fully pre-vaporized results (fully vaporized droplets in stoichiometric n-C_7H_{16}/air mixture with

FIG. 3. Time history of pressure, temperature, heat release rate, H_2O mass fraction, and droplet diameter of stoichiometric n-C_7H_{16}/air mixture with droplets. $\alpha_{d,0} = 8.0 \times 10^{-4}$ and $T_0 = 1000$ K.
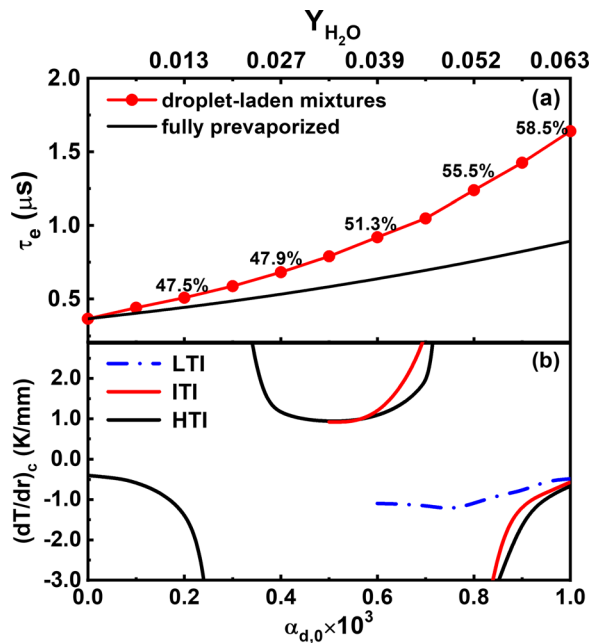
FIG. 5. (a) Excitation time and (b) critical temperature gradient as functions of initial volume fraction. $T_0 = 1000$ K. Y_{H2O} along the top axis indicates the water vapor mass fraction when the droplets are fully vaporized.

temperature of 1000 K. Water steam mass fractions Y_{H2O} marked at the top x axis) are also added. It is seen from Fig. 5(a) that the excitation time τ_e increases monotonically with $\alpha_{d,0}$. As known from our previous work,[44] τ_e monotonically decreases (increases) with initial temperature (H$_2$O mole fraction). This means that both evaporative cooling and water vapor dilution can lead to a larger τ_e. Note that the degree of cooling or dilution is related to $\alpha_{d,0}$. Therefore, τ_e increases monotonically with $\alpha_{d,0}$. The difference of τ_e between droplet-laden and fully pre-vaporized mixtures is caused by the cooling effect. The relative errors of excitation time, corresponding to some selected $\alpha_{d,0}$, induced by cooling effect are marked in Fig. 5(a). One can see that the cooling effect becomes more crucial with increased $\alpha_{d,0}$.

Figure 5(b) shows the critical temperature gradient as a function of initial volume fraction. It is noted that the critical temperature gradient is associated with ignition delay time [see Eq. (26)]. Thus, for multi-stage autoignition, the critical temperature gradient of different stages can be obtained. It is seen from Fig. 5(b) that three branches of the critical temperature gradient of HTI exist, and a negative (positive) value of $(dT/dr)_c$ indicates that a hot (cold) spot is required for simulations of inhomogeneous mixture in Sec. V. In addition, two branches of the critical temperature gradient of ITI are observed, whilst only one branch exists for the critical temperature gradient of LTI.

B. Chemical explosive mode analysis

To further understand the multi-stage autoignition of two-phase n-C$_7$H$_{16}$/air mixture, Fig. 6 shows the time evolutions of the real part of the eigenvalue of chemical Jacobian matrix, Re(λ_e), and EIs of the dominant species. It corresponds to the results in Fig. 3. It is seen that zero-crossing of Re(λ_e) is observed for the LTI and HTI events. This is
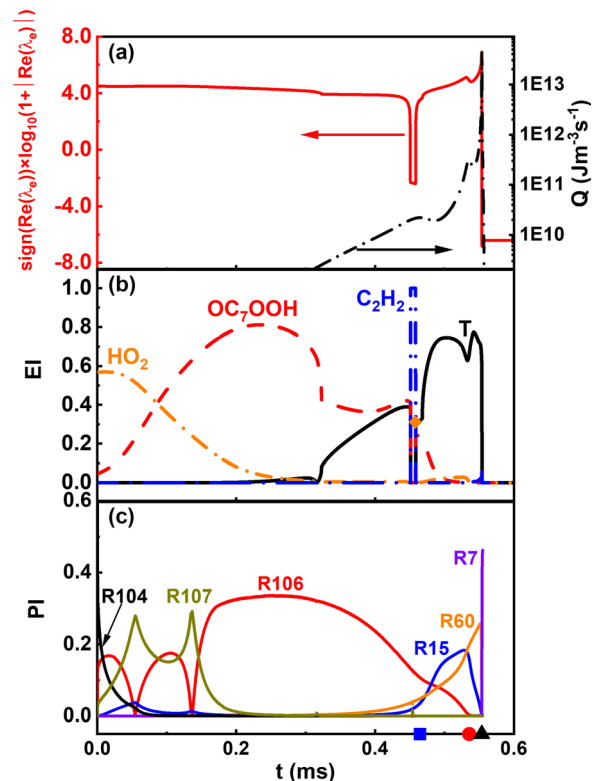
FIG. 6. Time evolutions of (a) real part of eigenvalue Re(λ_e), heat release rate, (b) EI's, and (c) PI's of dominant elementary reactions. $\alpha_{d,0} = 8.0 \times 10^{-4}$ and $T_0 = 1000$ K. Orange diamond in (b): onset of thermal runaway process. Symbols on x axis: blue square: $\tau_{ig,1}$; red circle: $\tau_{ig,2}$; black triangle: $\tau_{ig,3}$.

also observed in Refs. 66 and 72 for n-heptane autoignition. Moreover, as seen from Fig. 6(b), the contributions of HO$_2$ or OC$_7$OOH (KET) toward CEM are dominant prior to the LTI. Nevertheless, when LTI is initiated, C$_2$H$_2$ becomes most important. This indicates that the LTI is mainly controlled by radical proliferation (chemical runaway).[65–67] After LTI, the temperature contribution becomes dominant (see red circles in Fig. 6), corresponding to the thermal runaway process.[65–67]

To reveal the contributions of the individual elementary reactions toward the CEM, Fig. 6(c) shows the time evolutions of the PI's of dominant elementary reactions. The related chemical reactions are listed in Table I, with dominant reactions at each ignition stage also marked. It is seen from Fig. 6(c) that, before LTI (marked as a solid square along the time axis), R104, R106, and R107 (see reactions in Table I) are dominant, which correspond to n-C$_7$H$_{16}$ oxidation and generation of R, RO$_2$, and QOOH, indicating that the low-temperature chemistry is crucial during this period. After LTI, C$_0$ (R7 and R15) and C$_2$ (R60) oxidation become dominated during ITI and HTI. As such, the results in Fig. 6(c) further confirm the multi-stage ignition induced by the evaporation of dispersed ultrafine water droplets with intermediate or high loadings (see Fig. 4). The CEMA results of droplet-free mixtures can be seen in the supplementary material (i.e., Fig. S2), and one can see that only HTI event exists, which further confirms the role of the droplet evaporation in inducing the multi-stage ignitions.

TABLE I. Dominant elementary reactions identified with CEMA. Dominant elementary reactions at each ignition delay instant are highlighted using boldface.

Index	Reaction
R7	**H + OH + M <=> H$_2$O + M (HTI)**
R15	2OH + M <=> H$_2$O$_2$ + M
R60	**C$_2$H$_3$ + O$_2$ => CH$_2$O + HCO (ITI)**
R104	NXC$_7$H$_{16}$ + O$_2$ => SXC$_7$H$_{15}$ + HO$_2$ (RH + O$_2$ => R + HO$_2$)
R106	**SXC$_7$H$_{15}$ + O$_2$ <=> PC$_7$H$_{15}$O$_2$ (LTI)** **(R + O$_2$ <=> RO$_2$)**
R107	PC$_7$H$_{15}$O$_2$ => PHEOOHX$_2$ (RO$_2$ => QOOH)

V. REACTION FRONT DEVELOPMENT FROM AN IGNITION SPOT IN TWO-PHASE MIXTURES

A. Reaction front initiation mode

Figure 7 summarizes the reaction front initiation modes from our 1D numerical simulations with an ignition spot. They are identified based on the relations between gas temperature $T_{i,0}$ and lower turnover temperature T_l. It is seen from Fig. 2(a) that the corresponding lower turnover temperature, T_l, is 1000 K at about $\alpha_{d,0} = 8.0 \times 10^{-4}$, which equals the initial gas temperature outside the ignition

spot, $T_{i,0}$. In addition, the effect of droplet volume fraction on turnover temperature is also shown in Fig. 4(b). Below are the descriptions for the various modes:

(1) If $T_{i,0}$ is close to T_l [see Fig. 7(a)], then the ignition delay time at the right end of the ignition spot, $\tau_{ig,3}(T_{i,0})$, is always shorter than that at the left, $\tau_{ig,3}(T_0(r=0))$, regardless of negative or positive temperature gradient inside the spot. Therefore, autoignition is initiated at the right of the ignition spot, and the HTI waves travel from right to left within the ignition spot, leading to an implosion over the ignition spot. This is termed as mode a.

(2) If $T_{i,0}$ is slightly higher (lower) than T_l [Figs. 7(b) and 7(c)], then a cold (hot) spot is required to initiate the reaction front. One can see that the lower turnover temperature T_l is reached at some locations inside the ignition spot. Thus, the HTI waves are initiated inside the ignition spot, and subsequently, two oppositely propagating HTI waves are formed. Figures 7(b) and 7(c) correspond to modes b and c.

(3) If the initial end gas temperature $T_{i,0}$ is sufficiently higher (lower) than T_l [Figs. 7(d) and 7(e)], then the gas temperature reduced by droplet evaporation is beyond the NTC temperature range. As such, the HTI waves are initiated at the left boundary of the ignition spot and propagate rightward. They are modes d and e.
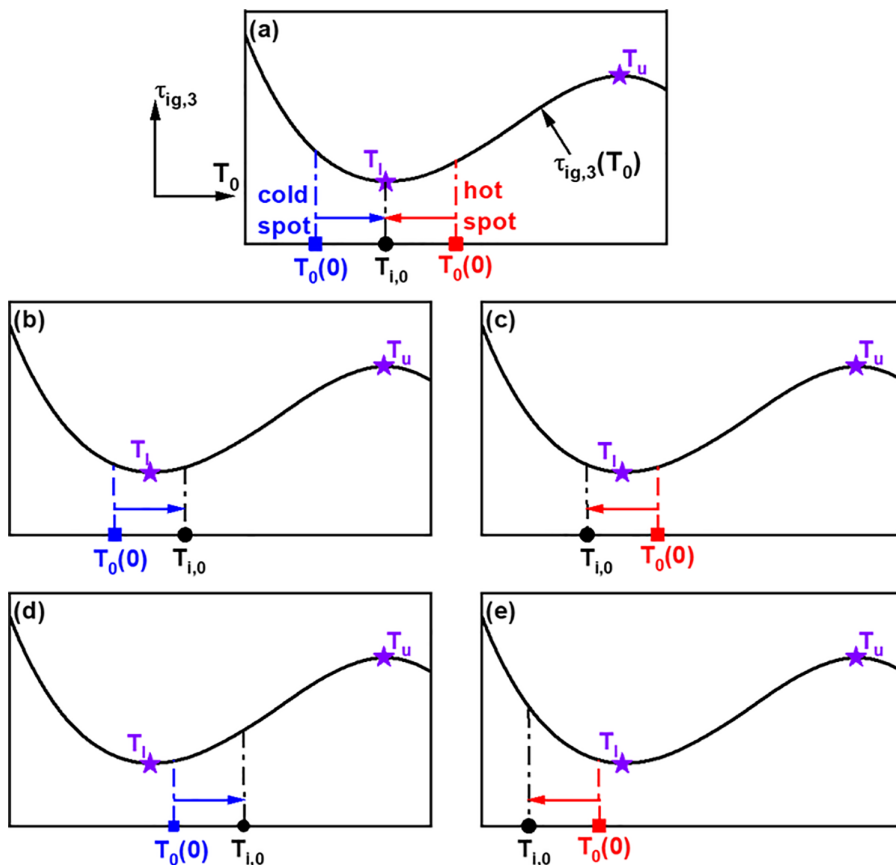
FIG. 7. Reaction front initiation mode: (a) $T_{i,0}$ is close to T_l [i.e., $T_0(0) < T_{i,0} \approx T_l$ or $T_{i,0} \approx T_l < T_0(0)$], (b) $T_{i,0}$ is slightly higher than T_l [$T_0(0) < T_l < T_{i,0}$], (c) $T_{i,0}$ is slightly lower than T_l [$T_{i,0} < T_l < T_0(0)$], (d) $T_{i,0}$ is sufficiently higher than T_l [$T_l < T_0(0) < T_{i,0}$], and (e) $T_{i,0}$ is sufficiently lower than T_l [$T_{i,0} < T_0(0) < T_l$]. $T_{i,0}$ is initial gas temperature outside the ignition spot, whereas $T_0(0)$ is the initial gas temperature at the left boundary.

Figure 8 further characterizes the reaction front initiation mode in terms of reaction front propagating direction and speed, under various temperature gradients and droplet volume fractions. The temperature gradient is normalized based on the maximum one of the corresponding volume fractions, that is, $(dT_0/dr)_{\alpha_{d,0},\max}$. In general, through increasing the value of initial temperature gradients (dT_0/dr), reaction front initiation mode changes from supersonic front to subsonic one. Here, the supersonic and subsonic conditions are determined based on the ratio between the average propagation speed S_{AVG} of the reaction front and the sound speed predicted based on the initial thermochemical properties in the middle of the ignition spot. If the ratio is greater than one, then it is supersonic; otherwise, it is subsonic. For a constant $\alpha_{d,0}$, the $(dT_0/dr)_{\alpha_{d,0},\max}$ is selected, such that it is large enough to cover all the possible reaction front initiation modes. In other words, the corresponding reaction front initiation mode of $(dT_0/dr)_{\alpha_{d,0},\max}$ is subsonic. For instance, they are 25.71, −11.79, and −9.98 K/mm for $\alpha_{d,0} = 8.0 \times 10^{-4}$, 9.0×10^{-4}, and 1.0×10^{-3}, respectively. Note that $(dT_0/dr)_{\alpha_{d,0},\max}$ is different from the critical temperature gradient from 0D calculations $(dT/dr)_c$. It is seen that the autoignition waves initiated at the left end of the ignition spot [i.e., mode d and e in Figs. 7(d) and 7(e)] are found for most occasions (square and diamond symbols). Furthermore, when the temperature gradient is increased, the propagation speed of the autoignition wave is changed from supersonic to subsonic conditions for a constant droplet loading, for example, $\alpha_{d,0} = 2.0 \times 10^{-4}$. This is because the interaction between pressure wave generated by heat release rate and autoignition wave is weakened. In addition, the autoignition wave from the right end of the ignition spot [i.e., mode a in Fig. 7(a)] is found for $\alpha_{d,0} = 8.0 \times 10^{-4}$, because the corresponding initial gas temperature outside the ignition spot is almost equal to the lower turnover temperature. Furthermore, change of the reaction front initiation mode is also found for $\alpha_{d,0} = 7.0 \times 10^{-4}$ and 9.0×10^{-4}. With a higher initial temperature gradient, autoignition waves traveling toward both left and right sides [i.e., mode b and c in Figs. 7(b) and 7(c)] are observed. This is because the lower turnover temperature T_l is reached at some locations inside the ignition spot as described in Figs. 7(b) and 7(c).
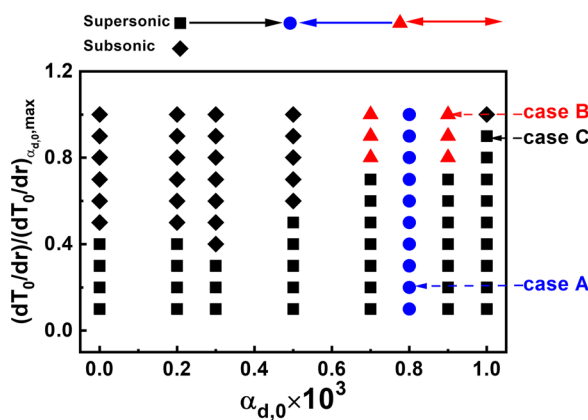
FIG. 8. Reaction front initiation mode in the diagram of ignition spot temperature gradient vs droplet volume fraction. $d_0 = 5 \, \mu m$ and $T_0 = 1000$ K. Ignition spot size is $r_0 = 3.5$ mm. Black diamonds: subsonic wave from left to right, black squares: supersonic wave from left to right, blue circles: from right to left, and red triangles: for middle to both sides.

Whether the results from the two-phase gas-droplets can be accommodated in the Bradley's diagram[13,14] will be discussed in Sec. V E.

B. Reaction front development within the ignition spot

Reaction front development within an ignition spot in two-phase medium will be studied in this section, through three representative cases, that is, A, B, and C, tabulated in Table II and marked in Fig. 8. Their spot radii are $r_0 = 3.5$ mm, and their droplet volume fractions are 8.0×10^{-4}, 9.0×10^{-4}, and 1.0×10^{-3}, respectively. Specifically, a cold spot (i.e., $dT_0/dr > 0$) is needed for case A, whilst a hot spot (i.e., $dT_0/dr < 0$) for cases B and C. The corresponding temperature gradient and reaction front initiation mode of cases A−C are listed in Table II.

To reveal the effects of droplet evaporation on the change of temperature gradient within the ignition spot ($r/r_0 \leq 1$) before ignition, Fig. 9 shows the spatial distributions of the gas temperature gradients in cases A–C when all droplets are critically vaporized in the reactor. Apparently, the distributions of temperature gradient at $r/r_0 < 0.8$ are nearly uniform (consistently varies), and the corresponding values are almost 80% of their respective initial temperature gradients (marked as symbols along the y axis). It is noted that the gas temperature gradients may be affected by convection, diffusion, and droplet evaporation (chemical heat release is still weak at this stage). To find out the dominant factor, frozen droplet-free mixtures are considered. We conducted nonreacting droplet-free numerical experiments with same gas mixtures and temperature gradients of cases A–C. Thus, the gas temperature gradients can only be affected by convection and diffusion in these cases. Their counterpart results are also shown in Fig. 9. For the chemically frozen droplet-free mixtures, the corresponding values of gas temperature gradient at $r/r_0 < 0.8$ are almost the same as the respective initial values. Therefore, one can confirm that the major reason for temperature gradient reduction at $r/r_0 < 0.8$ is the difference of droplet evaporation caused by initial gas temperature distribution. In addition, the distributions of temperature gradient at $r/r_0 \geq 0.8$ are mainly controlled by the effects of diffusion, caused by the differences of temperature near the vicinity of the ignition spot.

Figures 10–12 show the temporal evolutions of temperature and mass fractions of key species within the ignition spot ($r < r_0$) for cases A–C. The zero-crossing points (marked as symbols) of the eigenvalue $\text{Re}(\lambda_e)$ denote the reaction fronts.[65–68] Line #1 corresponds to the early stage of autoignition when the whole droplets in the 1D reactor are critically vaporized. The corresponding temperature gradients are shown in Fig. 9. Lines #2 and #3 correspond to the instants of LTI and ITI at the midpoint of the ignition spot, whilst the rest visualize the HTI process. In Fig. 10, the gas temperature at early stage (line #1) and LTI (line #2) is below 1000 K due to the heat absorption by the

TABLE II. Information of cases A–C.

Case	α_d	dT_0/dr (K/mm)	Reaction front initiation mode
A	8.0×10^{-4}	5.14	a
B	9.0×10^{-4}	−11.79	c
C	1.0×10^{-3}	−7.98	e
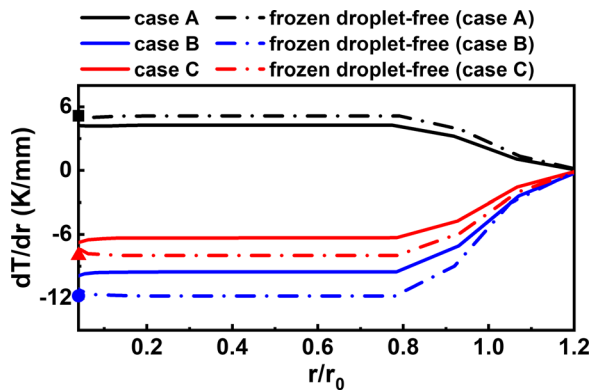
FIG. 9. Spatial distributions of gas temperature gradient when the droplets are critically vaporized. The corresponding initial gas temperature gradients of cases A–C are marked as symbols on the y axis.

evaporating droplets. It is noted that two zero-crossing points for the eigenvalue $Re(\lambda_e)$ are found at LTI, respectively, located at $r \approx 0.11 r_0$ and $0.24 r_0$ of line #2, which are associated with NTC. As we can see from Fig. 6(a), zero-crossing of $Re(\lambda_e)$ is also observed at LTI in the 0D results. At ITI (line #3), the maximum gas temperature within the ignition spot is about 1200 K. For the developments of HTI, autoignition occurs near the right end of the ignition spot (line #4). Subsequently, an autoignition wave travels from right to left within the ignition spot, that is, mode a as indicated in Fig. 7.

The NTC phenomenon initiated by the droplet evaporation cooling can also be confirmed through the evolutions of key species. For instance, the mass fractions of H_2O_2 and OC_7OOH reach their peaks around LTI (line #2) in the ignition spot, indicating that low-

temperature chemistry proceeds during this period. In addition, OH radical is accumulated since ITI (line #3). For HTI process, the peak value of H_2O_2 mass fraction is two orders of magnitude less than that at LTI. The OH mass fraction reaches its peak and evolves as the HTI wave propagates outwardly.

Figure 11 shows the counterpart results from case B, which corresponds to mode c. Compared with case A, similar profiles of temperature are found before HTI (lines #1–3). At ITI (line #3), the maximum gas temperature within the ignition spot is about 1162 K. However, the HTI occurs inside the ignition spot located at $r/r_0 \approx 0.4$ (line #4). Subsequently, two autoignition waves are generated and propagate oppositely (line #5). Note that the temperature of the left-propagating autoignition wave is slightly higher due to the wall compression effects (line #5). Finally, the left-propagating autoignition wave disappears when the reactive gas is fully consumed near the left wall. In terms of the key radicals, corresponding profiles before HTI (lines #1–3) are found to be similar with those of case A. For the HTI development, the OH mass fraction reaches its peak inside the ignition spot and evolves both leftward and rightward when the HTI waves propagate.

Moreover, Fig. 12 shows the counterpart results from case C (Mode e). Before HTI (lines #1–3), the evolutions of temperature and radicals are also similar with those of cases A and B. The maximum gas temperature within the ignition spot at ITI (lines 3) is about 1236 K. It is seen that the HTI occurs first at the left end (line #4). Accordingly, the right-ward propagating autoignition wave is observed (lines #5–8), which can be confirmed by the histories of both temperature and OH mass fraction.

One can see from Figs. 10–12 that multi-stage ignition occurs in the foregoing three initiation modes. Figure 13 shows the time history of heat release rate and pressure gradient from a probe at the middle of the ignition spot (i.e., $r = r_0/2$) in cases A–C. The pressure gradient
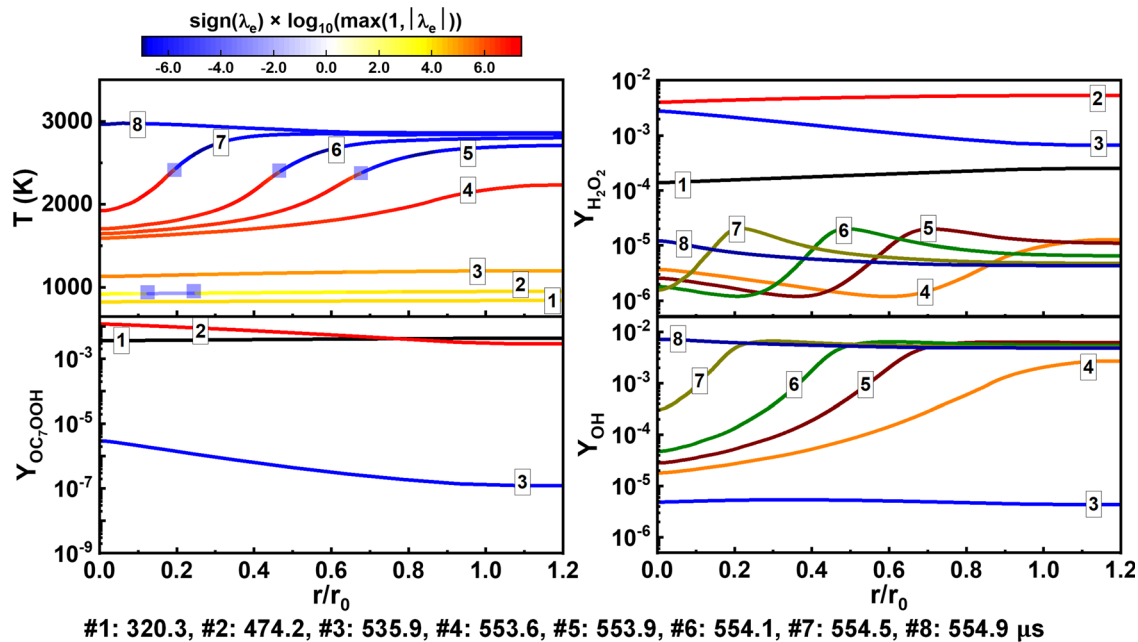
FIG. 10. Temporal evolutions of temperature and key species mass fractions within the ignition spot in case A. Symbols: zero-crossings of the eigenvalue $Re(\lambda_e)$.
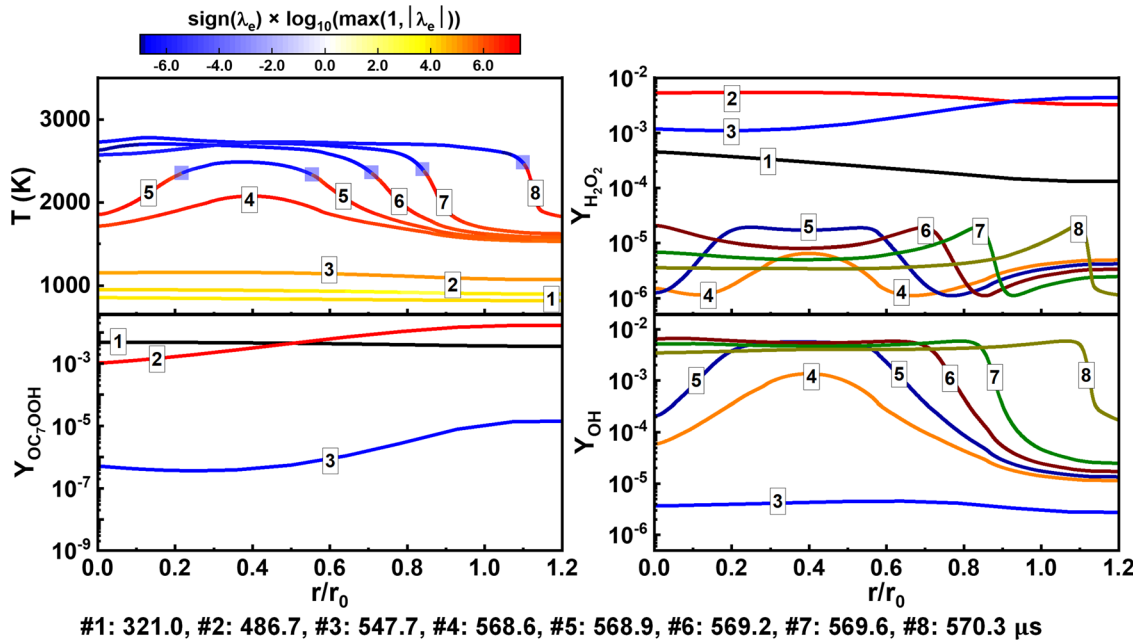
FIG. 11. Temporal evolutions of temperature and key species mass fractions within the ignition spot in case B. Symbol legend same as in Fig. 10.

history is shown to visualize the pressure wave development. Three pressure waves are observed from Fig. 13(b), corresponding to the three-stage ignition process shown in Fig. 13(a). They can be termed as LTI, ITI, and HTI pressure waves from left to right, respectively.

We can see that the magnitudes of LTI pressure wave and ITI pressure wave are at least two orders lower than that of HTI pressure wave. Thus, the HTI pressure wave is more important, which is a key factor for autoignition and detonation development.
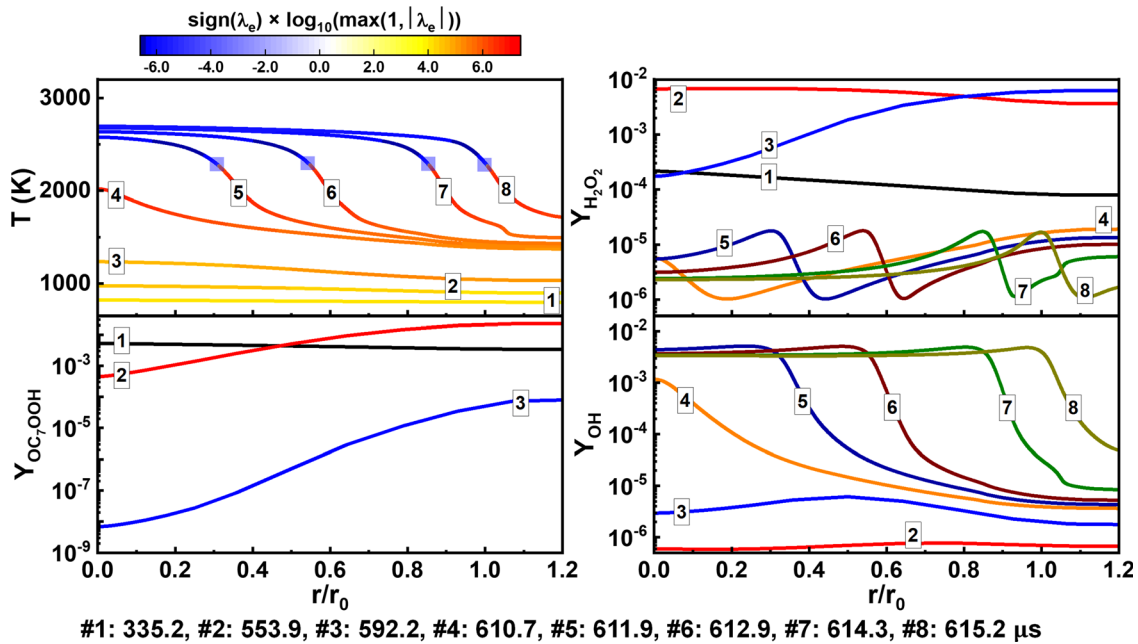
FIG. 12. Temporal evolutions of temperature and key species mass fractions within the ignition spot in case C. Symbol legend same as in Fig. 10.
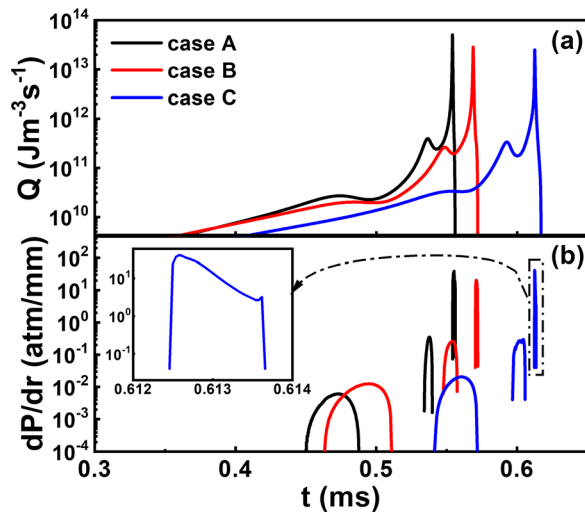
FIG. 13. Time history of (a) heat release rate and (b) pressure gradient of cases A to C.

C. Reaction front propagation

Figure 14 shows the reaction front propagation speed in cases A–C. The reaction front is extracted from the location with maximum heat release rate. One can see that, in case A, the autoignition wave induced by thermal explosion near the right end of the spot ($r/r_0 = 1$) has a very high initial speed. It travels supersonically from right to left within the ignition spot. Near the left wall, the speed first increases and then decreases quickly to zero. The increase is caused by the wall compression effects, whilst the reduction at $r/r_0 < 0.053$ is because the reactive gas is gradually consumed near the left boundary.

In case B, autoignition wave is initiated at $r/r_0 \approx 0.39$. Two opposite autoignition waves are formed. On one hand, the rightward propagating wave speed is supersonic, but lower than the C–J speed. The reaction front accelerates abruptly when the autoignition of mixture near the right boundary occurs (i.e., $r/r_0 \approx 1.4$ in case B). On the other hand, the leftward propagating wave is faster, and the average speed is about 3000 m/s and finally decays near the left wall. The latter is faster because of the higher local heat release caused by the compression effect.
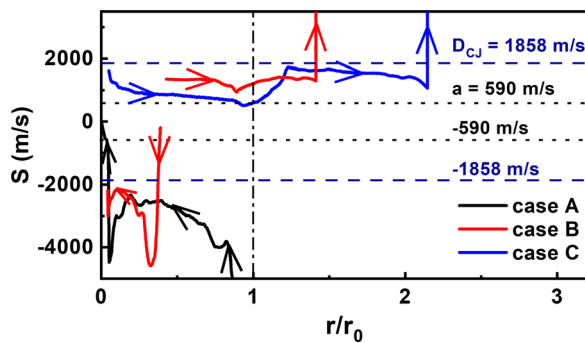
FIG. 14. Reaction front propagation speed as a function of radial coordinate in cases A–C. D_{CJ} is the C–J speed, and a is the sound speed.

In case C, the reaction front within the ignition spot propagates supersonically and the average propagation speed is about 800 m/s. The reaction front accelerates to the C–J speed outside the ignition spot. The predicted wave speed in case C is approximately 1525 m/s. It is lower than the C–J speed of stoichiometric droplet-free n-C_7H_{16}/air mixtures. That may be because of the curvature effects from the spherical geometry,[73,74] partial reaction of the end gas before the arrival of the detonation wave, and/or the dilution (mass transfer) and cooling (heat transfer) induced by water droplets evaporation. Note that inter-phase momentum exchange is not possible since the droplets have been fully gasified before autoignition. Finally, the reaction front accelerates abruptly when the autoignition of mixture near the right boundary occurs (i.e., $r/r_0 \approx 2.1$ in case C).

D. Thermal state

To analyze the interactions between chemical reaction and pressure waves, Fig. 15 shows the evolutions of thermal states of cases A to C, which are extracted with the aid of a Lagrangian particle initially at the midpoint of the ignition spot. The position of the particle is updated in each time step based on the local flow speed. Therefore, the instantaneous thermal states (e.g., pressure, density, and heat release rate) at the particle position can be obtained from linear extrapolation of the gas properties.[25,75] Here, points a, b, and c in Fig. 15 denote three ignition stages of LTI, ITI, and HTI, respectively. In case A, within the ignition spot, one can see from the curves of $P-v$ and $P-t$ that the fluid particle undergoes continuous compression − expansion processes before the HTI occurs (i.e., the part before point c). This is because the joint influences of pressure pulse and NTC phenomenon. It is noted that the compression is dominant during LTI and ITI stages. During the transition from ITI to HTI (i.e., part bc on each curve), the gas at the particle location is compressed intensively with rapidly increased pressure. Meanwhile, the heat release rate increases rapidly and reaches the maximum value when HTI occurs (i.e., point c on the $Q-t$ curve). After HTI, the pressure keeps increasing and finally reaches its equilibrium value (see the $P-t$ curve), because the thermal explosion is achieved.

In cases B and C, continuous compression–expansion processes are also observed before the occurrence of HTI (i.e., before point c). However, the expansion is dominant during LTI and ITI stages both for case B and C, which is different from case A. During the transition from ITI to HTI (i.e., part bc), the fluid around the particle in case B is expanded, whilst in case C is compressed. This is because two opposite autoignition waves are formed within the ignition spot in case B. It is seen from Fig. 11 that the HTI first occurs at $r \approx 0.4r_0$. Therefore, influenced by the leftward propagating wave, the gas at the midpoint is initially expanded. Nevertheless, detonation does not develop when the pressure wave passes the particle in cases A–C. Therefore, only moderate interactions between chemical reaction and pressure wave occur.

E. Bradley's diagram for two-phase mixtures

Two parameters are used by Bradley and his co-workers[13,14] to characterize the interactions between the reaction wave and acoustic wave within the ignition spot in gaseous mixtures. The first one is the normalized temperature gradient ξ, which is the ratio of local sound speed to autoignition front propagation speed and measures the
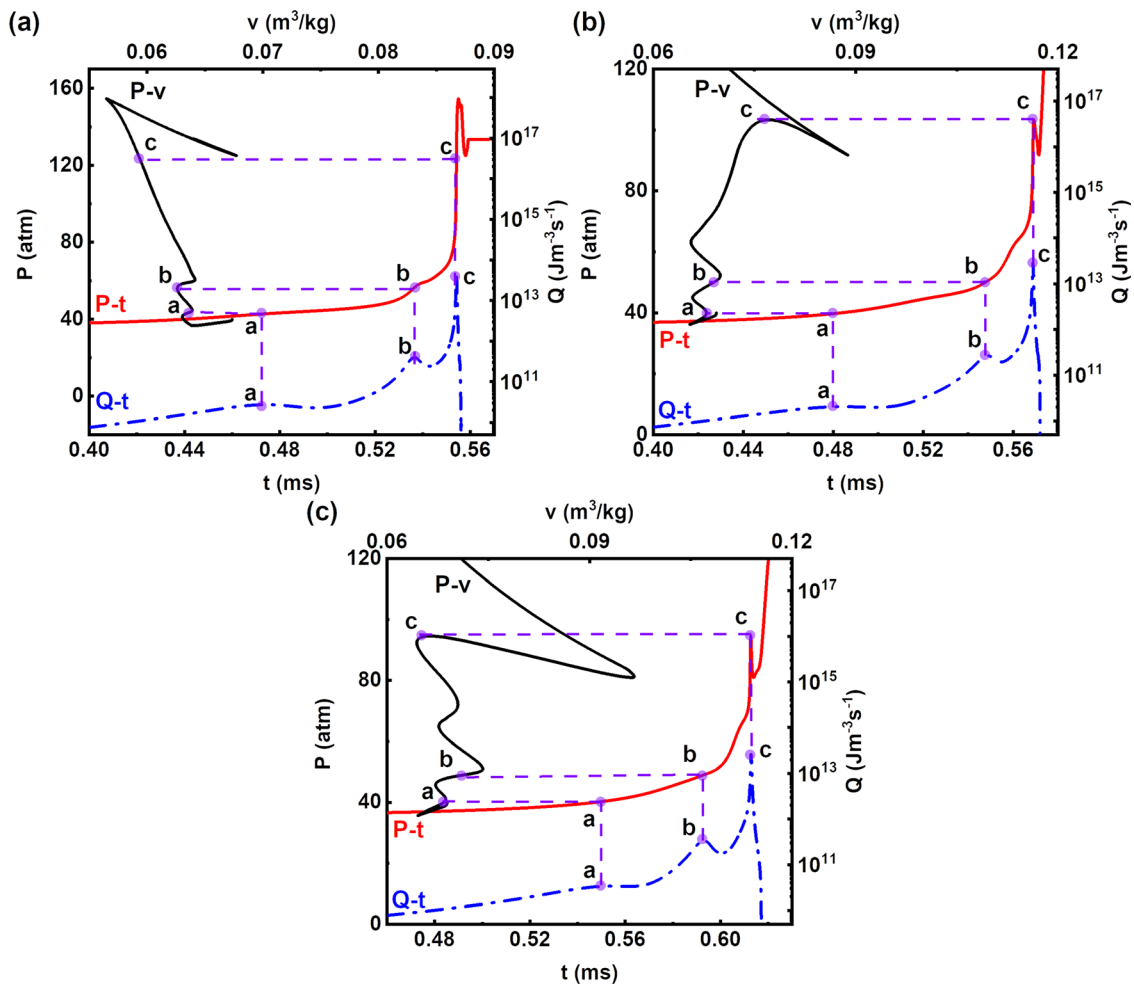
FIG. 15. Evolution of thermal states of a particle initially at midpoint of the ignition spot (i.e., $r = r_0/2$) of cases (a) A, (b) B, and (c) C. $P-v$ (pressure vs specific volume), $P-t$ (pressure vs time), and $Q-t$ (heat release rate vs time) curves are shown.

coupling between the local autoignition and acoustic wave caused by the heat release (or *acoustic−induction coupling*[76]). It reads

$$\xi = \frac{dT_0/dr}{(dT_0/dr)_{c,\,r_0/2}}. \tag{27}$$

Here, $(dT_0/dr)_{c,\,r_0/2}$ is the critical temperature gradient, from Eq. (26). The subscript "$r_0/2$" indicates the quantity is estimated based on the initial thermochemical properties in the middle of the ignition spot. Note that dT_0/dr is the initial temperature gradient within the ignition spot [see Eq. (20)].

In addition, the second parameter, ε, is used to measure the timescale of reaction heat release relative to the residence time of the acoustic wave in the ignition spot (or *acoustic−exothermicity coupling*). It is defined as the ratio of acoustic time to excitation time, that is,

$$\varepsilon = \frac{r_0/a_{r_0/2}}{\tau_e}, \tag{28}$$

where $a_{r_0/2}$ is the sound speed at the middle of the ignition spot. Here, τ_e is obtained from 0D calculations based on the properties at the middle of the ignition spot.

With the above two parameters (ξ and ε), the autoignition modes of two-phase stoichiometric n-C_7H_{16}/air mixtures due to temperature gradient in an ignition spot are presented in Fig. 16 (i.e., Bradley's diagram). Note that only the autoignition waves formed at the left boundary of the ignition spot and traveling from left to right (modes d and e) are shown. The detonation limits of droplet-free mixtures diluted by H_2O vapor from our previous work[44] are also plotted here, and the volume fractions for them are converted from the mole fractions of H_2O vapor. Normalized maximum pressure P_{max}/P_e (with P_{max} and P_e being the maximum pressure from 1D calculations and equilibrium pressure from 0D constant-volume calculations, respectively) is used to identify different categories. It is seen from Fig. 16(a) that, for $\varepsilon = 3.6$, 7.5, 10.1, 11.7, and 16.2 (corresponds to droplet-free mixtures), three categories are identified when ξ increases: (I) supersonic deflagrative wave, (II) detonative wave with high maximum pressure ($P_{max}/P_e \geq 2$, red symbols in Fig. 16), and (III) subsonic
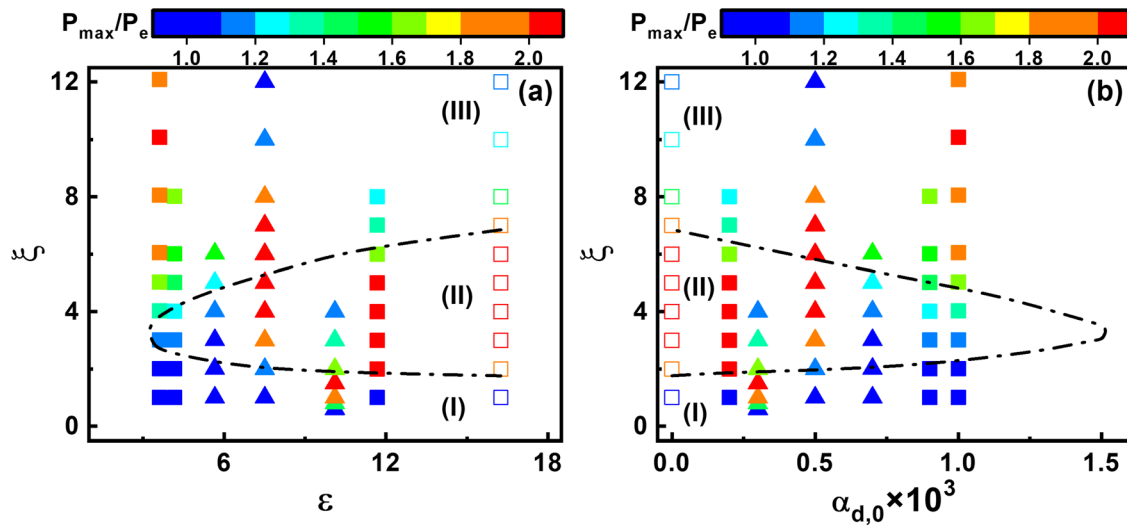
FIG. 16. Autoignition mode of stoichiometric n-C_7H_{16}/air mixtures with water droplets in (a) $\xi - \varepsilon$ and (b) $\xi - \alpha_{d,0}$ diagrams. Hollow squares: droplet-free cases initialized by hot spot; solid squares: two-phase cases initialized by hot spot; solid triangles: two-phase cases initialized by cold spot; dashed lines: detonation limits of n-C_7H_{16}/air mixtures with water vapor.[44]

deflagrative wave. This is consistent with what are found in gaseous mixtures.[44] However, the detonation regions change significantly and non-monotonically with ε. For example, the regional center of detonation mode is $\xi \approx 4.5$ for $\varepsilon = 16.2$, $\xi \approx 1.5$ for $\varepsilon = 10.1$, and $\xi \approx 10.0$ for $\varepsilon = 3.6$, respectively. This indicates that the effects of water droplets on ξ is not monotonic, which is related to the change of $(dT_0/dr)_{c,r_0/2}$ due to ultrafine water droplet evaporation.

Furthermore, for $\varepsilon = 4.2$ and 5.7, only supersonic deflagrative waves are found. Two opposite autoignition waves are formed when keeping increasing ξ for the corresponding ε [see Figs. 7(b), 7(c), and 10], which are not shown in Fig. 16. The distributions of the corresponding results are reversed in $\xi - \alpha_{d,0}$ in Fig. 16(b). This is because a higher droplet volume fraction $\alpha_{d,0}$ corresponds to a higher excitation time τ_e, thus a lower ε, as shown in Eq. (28) and Fig. 5(a). Thus, one can see that, unlike the detonation limits of water droplet free mixtures (the dashed-dotted lines in Fig. 16), those of two-phase mixtures are not peninsular-shaped, as they are for gaseous mixtures.[14,17,26–28] Therefore, the applicability of the $\xi - \varepsilon$ diagram for a wider range of droplet-laden mixtures merits further studies, due to the significant influences of the evaporating disperse phase (e.g., water or fuel spray mists) for the thermochemical property in the ignition spot. In addition, the effects of water evaporation on Bradley's diagram have been further clarified under a higher initial temperature $T_0 = 1200$ K. The results are shown in the supplementary material (i.e., Fig. S3). Although the influence of NTC region variation is eliminated, the two-phase Bradley's diagram is qualitatively different from the purely gaseous ones.

VI. CONCLUSION

The effects of low-temperature chemistry induced by ultrafine water droplet evaporation on reaction front development from an ignition spot with temperature gradient are studied in this work. The Eulerian–Eulerian method is used to simulate the gas—liquid two-phase reactive flows and the physical model is one-dimensional

spherical reactor filled with stoichiometric gaseous n-C_7H_{16}/air mixture and ultrafine water droplets (initial diameter $5\,\mu$m). The main findings are summarized below.

The results from the homogeneous autoignition in two-phase mixtures show that the dependence of ignition delay on initial gas temperature is considerably affected by the water droplet evaporation. The turnover temperatures for NTC range increase in the two-phase mixtures compared to those of the droplet-free mixtures and also increase with droplet volume fraction. It is seen that, due to the smallness of the water droplets, they complete the evaporation and hence considerably reduce the gas temperature before the ignition occurs. In addition, only high-temperature ignition is observed when the initial droplet volume fraction is less than 5.0×10^{-4}. Beyond that, multistage ignitions are induced by droplet evaporation. It is also found that the excitation time increases with droplet volume fraction. Moreover, as volume fraction increases, cold or hot spot is needed to initiate a reactive front. The CEMA analysis also unveils the low-temperature chemical reactions in the gas phase chemistry induced by the ultrafine droplet evaporation.

Through the one-dimensional simulations with ignition spot, we identify three modes for the origin of the reaction front, that is, left and right ends of ignition spot and inside it, based on the relations between gas temperature and turnover temperature for NTC range. The reaction front development corresponding to the above modes is discussed in detail. In addition, the HTI pressure wave associated with HTI is more important. The predicted right-ward propagating wave speed is lower than the C–J speed of stoichiometric droplet-free n-C_7H_{16}/air mixtures. Continuous compression—expansion processes are found from $P-v$ curve, which are induced by the joint influences of pressure pulse and NTC phenomenon. Moreover, autoignition modes are summarized in $\xi - \varepsilon$ and $\xi - \alpha_{d,0}$ diagrams. The detonation regions change significantly and non-monotonically with ε or $\alpha_{d,0}$. The detonation limits of two-phase mixtures are not regularly peninsular-shaped, like those for purely gaseous mixtures.

In this work, only ultrafine mono-sized water droplets are considered, which are completely gasified before ignition starts. Therefore, their direct interactions with the reaction front propagation and detonation are not present. Furthermore, the applicability of the $\xi - \varepsilon$ diagram for a wider range of droplet-laden mixtures needs to be further examined, due to the significant modulation from the evaporating disperse phase (e.g., water or fuel spray mists) for the thermochemical property in the ignition spot. These are interesting topics for our future studies.

SUPPLEMENTARY MATERIAL

See supplementary material for mesh sensitivity results, CEMA analysis of droplet-free mixtures and Bradley's diagram.

ACKNOWLEDGMENTS

APPENDIX: VALIDATION OF DROPLET HEATING AND EVAPORATION MODELS

Figure 17 shows the time history of temperature of single water droplet. In the experiment by Volkov and Strizhak,[77] one water droplet is placed in the air with temperature of 373 K and velocity of about 3 m/s. Two measurement techniques are used to determine the surface and internal droplet temperatures T_s and T_d (both included in Fig. 17), namely, planar laser-induced fluorescence (PLIF) and thermocouple. The droplet is not exactly spherical, and its volume is 10 μl (the corresponding nominal diameter is 2.67 mm).[77] In the simulation, we assume that the temperature
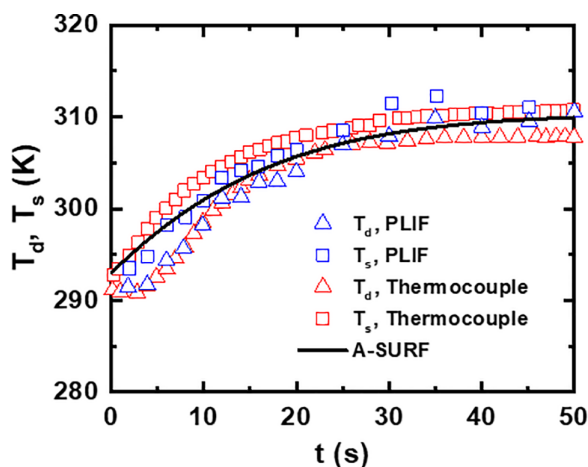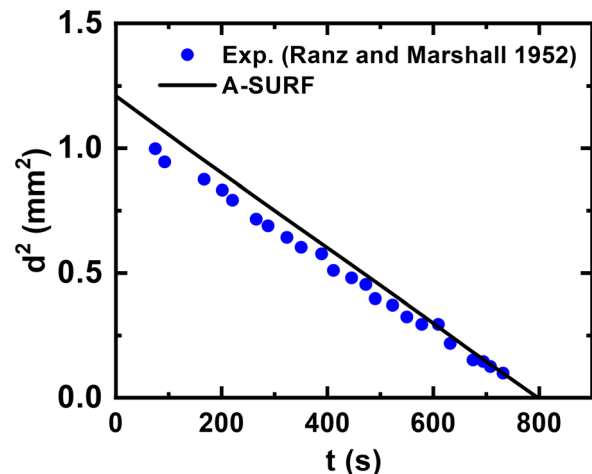
FIG. 18. Time history of the square of droplet diameter. Experimental data: Ranz and Marshall.[59]

inside the droplet is uniform, and the initial droplet diameter equals to the nominal diameter. It is seen from Fig. 17 that good agreement can be achieved about the overall evolutions of the droplet temperature and the equilibrium temperature around $t = 50$ s.

Figure 18 further compares the diameter evolution of an evaporating water droplet against the experimental data.[59] The initial diameter and temperature of the water droplet are 1.1 mm and 282 K, respectively. The temperature of the ambient gas is 298 K. Excellent agreement is found between the present simulations and the measured data. In addition, the slope (i.e., evaporation coefficient) computed by A-SURF is -1.51×10^{-3} mm^2/s, close to that from experimental data (-1.37×10^{-3} mm^2/s). In general, the evaporation model in A-SURF can accurately predict the droplet evaporation in terms of the evaporation coefficient and the diameter decaying history.

DATA AVAILABILITY

The data that support the findings of this study are available from the corresponding author upon reasonable request.

REFERENCES

[1]Z. Wang, H. Liu, and R. D. Reitz, "Knocking combustion in spark-ignition engines," Prog. Energy Combust. Sci. **61**, 78 (2017).

[2]K. P. Grogan, S. S. Goldsborough, and M. Ihme, "Ignition regimes in rapid compression machines," Combust. Flame **162**, 3071 (2015).

[3]J. Rudloff, J. M. Zaccardi, S. Richard, J. M. Anderlohr, N. Peters, B. Kerschgens, G. Paczko, C. Dahnz, and U. Spicher, "Analysis of pre-ignition in highly charged SI engines: Emphasis on the auto-ignition mode," Proc. Combust. Inst. **34**, 2959 (2013).

[4]C. Dahnz and U. Spicher, "Irregular combustion in supercharged spark ignition engines–pre-ignition and other phenomena," Int. J. Engine Res. **11**, 485 (2010).

[5]N. Peters, B. Kerschgens, and G. Paczko, "Super-knock prediction using a refined theory of turbulence," SAE Int. J. Engines **6**, 953 (2013).

[6]H. Wei, X. Zhang, H. Zeng, R. Deiterding, J. Pan, and L. Zhou, "Mechanism of end-gas autoignition induced by flame-pressure interactions in confined space," Phys. Fluids **31**(7), 076106 (2019).

[7]M. Reynaud, F. Virot, and A. Chinnayya, "A computational study of the interaction of gaseous detonations with a compressible layer," Phys. Fluids **29**, 056101 (2017).

FIG. 17. Time history of the droplet temperature. Experimental data: Volkov and Strizhak.[77]

[8]Y. Liu, W. Zhou, Y. Yang, Z. Liu, and J. Wang, "Numerical study on the instabilities in H₂-air rotating detonation engines," Phys. Fluids **30**, 046106 (2018).

[9]Y. Fang, Y. Zhang, X. Deng, and H. Teng, "Structure of wedge-induced oblique detonation in acetylene-oxygen-argon mixtures," Phys. Fluids **31**, 026108 (2019).

[10]Z. Wang, H. Liu, T. Song, Y. Qi, X. He, S. Shuai, and J. Wang, "Relationship between super-knock and pre-ignition," Int. J. Engine Res. **16**, 166 (2015).

[11]Z. Wang, Y. Qi, X. He, J. Wang, S. Shuai, and C. K. Law, "Analysis of pre-ignition to super-knock: Hotspot-induced deflagration to detonation," Fuel **144**, 222 (2015).

[12]Y. B. Zeldovich, "Regime classification of an exothermic reaction with nonuniform initial conditions," Combust. Flame **39**, 211 (1980).

[13]D. Bradley, C. Morley, X. J. Gu, and D. R. Emerson, "Amplified pressure waves during autoignition: Relevance to CAI engines," SAE Trans. **111**, 2679–2690 (2002).

[14]X. J. Gu, D. R. Emerson, and D. Bradley, "Modes of reaction front propagation from hot spots," Combust. Flame **133**, 63 (2003).

[15]D. Bradley and G. T. Kalghatgi, "Influence of autoignition delay time characteristics of different fuels on pressure waves and knock in reciprocating engines," Combust. Flame **156**, 2307 (2009).

[16]D. Bradley, "Autoignitions and detonations in engines and ducts," Philos. Trans. R. Soc., A **370**, 689 (2012).

[17]J. Pan, S. Dong, H. Wei, T. Li, G. Shu, and L. Zhou, "Temperature gradient induced detonation development inside and outside a hotspot for different fuels," Combust. Flame **205**, 269 (2019).

[18]Y. Gao, P. Dai, and Z. Chen, "Numerical studies on autoignition and detonation development from a hot spot in hydrogen/air mixtures," Combust. Theory Modell. **24**, 245 (2020).

[19]J. Pan, H. Wei, G. Shu, Z. Chen, and P. Zhao, "The role of low temperature chemistry in combustion mode development under elevated pressures," Combust. Flame **174**, 179 (2016).

[20]J. Pan, H. Wei, G. Shu, and R. Chen, "Effect of pressure wave disturbance on auto-ignition mode transition and knocking intensity under enclosed conditions," Combust. Flame **185**, 63 (2017).

[21]H. Terashima and M. Koshi, "Mechanisms of strong pressure wave generation in end-gas autoignition during knocking combustion," Combust. Flame **162**, 1944 (2015).

[22]H. Terashima, A. Matsugi, and M. Koshi, "Origin and reactivity of hot-spots in end-gas autoignition with effects of negative temperature coefficients: Relevance to pressure wave developments," Combust. Flame **184**, 324 (2017).

[23]H. Terashima, A. Matsugi, and M. Koshi, "End-gas autoignition behaviors under pressure wave disturbance," Combust. Flame **203**, 204 (2019).

[24]P. Dai, Z. Chen, S. Chen, and Y. Ju, "Numerical experiments on reaction front propagation in n-heptane/air mixture with temperature gradient," Proc. Combust. Inst. **35**, 3045 (2015).

[25]P. Dai and Z. Chen, "Supersonic reaction front propagation initiated by a hot spot in n-heptane/air mixture with multistage ignition," Combust. Flame **162**, 4183 (2015).

[26]P. Dai and Z. Chen, "Effects of NOx addition on autoignition and detonation development in DME/air under engine-relevant conditions," Proc. Combust. Inst. **37**, 4813 (2019).

[27]P. Dai, C. Qi, and Z. Chen, "Effects of initial temperature on autoignition and detonation development in dimethyl ether/air mixtures with temperature gradient," Proc. Combust. Inst. **36**, 3643 (2017).

[28]P. Dai, Z. Chen, and X. Gan, "Autoignition and detonation development induced by a hot spot in fuel-lean and CO₂ diluted n-heptane/air mixtures," Combust. Flame **201**, 208 (2019).

[29]H. Yu and Z. Chen, "End-gas autoignition and detonation development in a closed chamber," Combust. Flame **162**, 4102 (2015).

[30]H. Yu, C. Qi, and Z. Chen, "Effects of flame propagation speed and chamber size on end-gas autoignition," Proc. Combust. Inst. **36**, 3533 (2017).

[31]J. Pan, G. Shu, P. Zhao, H. Wei, and Z. Chen, "Interactions of flame propagation, auto-ignition and pressure wave during knocking combustion," Combust. Flame **164**, 319 (2016).

[32]M. B. Luong, G. H. Yu, T. Lu, S. H. Chung, and C. S. Yoo, "Direct numerical simulations of ignition of a lean n-heptane/air mixture with temperature and composition inhomogeneities relevant to HCCI and SCCI combustion," Combust. Flame **162**, 4566 (2015).

[33]M. B. Luong, S. Desai, F. E. Hernández Pérez, R. Sankaran, B. Johansson, and H. G. Im, "A statistical analysis of developing knock intensity in a mixture with temperature inhomogeneities," Proc. Combust. Inst. **38**, 5781 (2021).

[34]F. Hoppe, M. Thewes, H. Baumgarten, and J. Dohmen, "Water injection for gasoline engines: Potentials, challenges, and solutions," Int. J. Engine Res. **17**, 86 (2016).

[35]A. Li, Z. Zheng, and T. Peng, "Effect of water injection on the knock, combustion, and emissions of a direct injection gasoline engine," Fuel **268**, 117376 (2020).

[36]S. Zhu, B. Hu, S. Akehurst, C. Copeland, A. Lewis, H. Yuan, I. Kennedy, J. Bernards, and C. Branney, "A review of water injection applied on the internal combustion engine," Energy Convers. Manage. **184**, 139 (2019).

[37]C. Wang, F. Zhang, E. Wang, C. Yu, H. Gao, B. Liu, Z. Zhao, and C. Zhao, "Experimental study on knock suppression of spark-ignition engine fuelled with kerosene via water injection," Appl. Energy **242**, 248 (2019).

[38]J. A. Harrington, "Water addition to gasoline–Effect on combustion, emissions, performance, and knock," SAE Trans. **91**, 1226–1251 (1982).

[39]N. Miganakallu, Z. Yang, R. Rogóż, ŁJ. Kapusta, C. Christensen, S. Barros, and J. Naber, "Effect of water-methanol blends on engine performance at borderline knock conditions in gasoline direct injection engines," Appl. Energy **264**, 114750 (2020).

[40]Y. Zhuang, Y. Sun, Y. Huang, Q. Teng, B. He, W. Chen, and Y. Qian, "Investigation of water injection benefits on downsized boosted direct injection spark ignition engine," Fuel **264**, 116765 (2020).

[41]Q. Meng, N. Zhao, and H. Zhang, "On the distributions of fuel droplets and in situ vapor in rotating detonation combustion with prevaporized n-heptane sprays," Phys. Fluids **33**(4), 043307 (2021).

[42]Z. Huang and H. Zhang, "On the interactions between a propagating shock wave and evaporating water droplets," Phys. Fluids **32**, 123315 (2020).

[43]Y. Zhuang, Q. Li, P. Dai, and H. Zhang, "Autoignition and detonation characteristics of n-heptane/air mixture with water droplets," Fuel **266**, 117077 (2020).

[44]Z. Yu, H. Zhang, and P. Dai, "Autoignition and detonation development induced by temperature gradient in n-C₇H₁₆/air/H₂O mixtures," Phys. Fluids **33**, 017111 (2021).

[45]R. J. Kee, F. M. Rupley, and J. A. Miller, "CHEMKIN-II: A Fortran chemical kinetics package for the analysis of gas phase chemical kinetics," Report No. SAND89-8009B, Sandia National Laboratories, Livermore, CA, USA, 1989.

[46]R. Kee, J. Grcar, M. Smooke, J. Miller, and E. Meeks, "PREMIX: A Fortran program for modeling steady laminar one-dimensional," Report No. SAND85-8249, Sandia National Laboratories, Livermore, CA, USA, 1985.

[47]Z. Chen, *Studies on the Initiation, Propagation, and Extinction of Premixed Flames* (Princeton University, Princeton, NJ, USA, 2009).

[48]M. Sanjosé, J. M. Senoner, F. Jaegle, B. Cuenot, S. Moreau, and T. Poinsot, "Fuel injection model for Euler–Euler and Euler–Lagrange large-eddy simulations of an evaporating spray inside an aeronautical combustor," Int. J. Multiphase Flow **37**, 514 (2011).

[49]L. Qiao, "Transient flame propagation process and flame-speed oscillation phenomenon in a carbon dust cloud," Combust. Flame **159**, 673 (2012).

[50]S. Eidelman and A. Burcat, "Evolution of a detonation wave in a cloud of fuel droplets. Part I. Influence of igniting explosion," AIAA J. **18**, 1103 (1980).

[51]A. Burcat and S. Eidelman, "Evolution of a detonation wave in a cloud of fuel droplets. Part II. Influence of fuel droplets," AIAA J. **18**, 1233 (1980).

[52]R. Blouquin and G. Joulin, "On the quenching of premixed flames by water sprays: Influences of radiation and polydispersity," Symp. (Int.) Combust. **27**, 2829 (1998).

[53]N. S. Belyakov, V. I. Babushok, and S. S. Minaev, "Influence of water mist on propagation and suppression of laminar premixed flame," Combust. Theory Modell. **22**, 394 (2018).

[54]B. Abramzon and W. A. Sirignano, "Droplet vaporization model for spray combustion calculations," Int. J. Heat Mass Transfer **32**, 1605 (1989).

[55]Q. Meng, M. Zhao, H. Zheng, and H. Zhang, "Eulerian–Lagrangian modelling of rotating detonative combustion in partially pre-vaporized n-heptane sprays with hydrogen addition," Fuel **290**, 119808 (2021).

[56]L. Schiller, "A drag coefficient correlation," Z. Ver. Dtsch. Ing. **77**, 318–320 (1935).

[57]S. Cheatham and K. Kailasanath, "Numerical modelling of liquid-fuelled detonations in tubes," Combust. Theory Modell. **9**, 23 (2005).

[58]B. E. Poling, J. M. Prausnittz, and J. P. O'Connell, *The Properties of Gases and Liquids*, 5th ed. (McGraw-Hill Education, 2001).

[59]W. E. Ranz and W. R. Marshall, "Evaporation from drops. Part I," Chem. Eng. Prog. **48**(3), 141–146 (1952).

[60]C. T. Crowe, J. D. Schwarzkopf, M. Sommerfeld, and Y. Tsuji, *Multiphase Flows with Droplets and Particles* (CRC Press, 2011).

[61]Z. Chen, "Effects of radiation and compression on propagating spherical flames of methane/air mixtures near the lean flammability limit," Combust. Flame **157**, 2267 (2010).

[62]M. Sun and K. Takayama, "Conservative smoothing on an adaptive quadrilateral grid," J. Comput. Phys. **150**, 143 (1999).

[63]S. Liu, J. C. Hewson, J. H. Chen, and H. Pitsch, "Effects of strain rate on high-pressure nonpremixed n-heptane autoignition in counterflow," Combust. Flame **137**, 320 (2004).

[64]M. Zhao, Z. Ren, and H. Zhang, "Pulsating detonative combustion in n-heptane/air mixtures under off-stoichiometric conditions," Combust. Flame **226**, 285 (2021).

[65]Z. Luo, C. S. Yoo, E. S. Richardson, J. H. Chen, C. K. Law, and T. Lu, "Chemical explosive mode analysis for a turbulent lifted ethylene jet flame in highly heated coflow," Combust. Flame **159**, 265 (2012).

[66]R. Shan, C. S. Yoo, J. H. Chen, and T. Lu, "Computational diagnostics for n-heptane flames with chemical explosive mode analysis," Combust. Flame **159**, 3119 (2012).

[67]T. F. Lu, C. S. Yoo, J. H. Chen, and C. K. Law, "Three-dimensional direct numerical simulation of a turbulent lifted hydrogen jet flame in heated coflow: A chemical explosive mode analysis," J. Fluid Mech. **652**, 45 (2010).

[68]W. Wu, Y. Piao, Q. Xie, and Z. Ren, "Flame diagnostics with a conservative representation of chemical explosive mode analysis," AIAA J. **57**, 1355 (2019).

[69]S. H. Lam and D. A. Goussis, "The CSP method for simplifying kinetics," Int. J. Chem. Kinet. **26**, 461 (1994).

[70]D. A. Goussis, H. G. Im, H. N. Najm, S. Paolucci, and M. Valorani, "The origin of CEMA and its relation to CSP," Combust. Flame **227**, 396 (2021).

[71]W. Ji, P. Zhao, T. He, X. He, A. Farooq, and C. K. Law, "On the controlling mechanism of the upper turnover states in the NTC regime," Combust. Flame **164**, 294 (2016).

[72]X. Zhang, C. Yuan, L. Zhou, W. Zhao, Z. Liu, and H. Wei, "Effects of initial temperature on ignition and flame propagation of dual-fuel mixture in mixing layer," Combust. Flame **225**, 468 (2021).

[73]H. D. Ng and J. H. S. Lee, "Direct initiation of detonation with a multi-step reaction scheme," J. Fluid Mech. **476**, 179 (2003).

[74]C. Qi and Z. Chen, "Effects of temperature perturbation on direct detonation initiation," Proc. Combust. Inst. **36**, 2743 (2017).

[75]R. Zhou and J. P. Wang, "Numerical investigation of flow particle paths and thermodynamic performance of continuously rotating detonation engines," Combust. Flame **159**, 3632 (2012).

[76]C. A. Z. Towery, A. Y. Poludnenko, and P. E. Hamlington, "Detonation initiation by compressible turbulence thermodynamic fluctuations," Combust. Flame **213**, 172 (2020).

[77]R. S. Volkov and P. A. Strizhak, "Planar laser-induced fluorescence diagnostics of water droplets heating and evaporation at high-temperature," Appl. Therm. Eng. **127**, 141 (2017).